Applied Physics A (2020) 126:607
https://doi.org/10.1007/s00339-020-03789-8

Applied Physics A
Materials Science & Processing

Effect of La^{3+} substitution on the physical properties of $CaTiO_3$–$0.15KNbO_3$-based lead-free ceramics

Ah. Dhahri[1] · Hend Kacem[2] · J. Dhahri[2]

Received: 2 May 2020 / Accepted: 4 July 2020 / Published online: 13 July 2020

Abstract
Polycrystalline samples $Ca_{0.85-x}La_xK_{0.15-x}Ti_{0.85}Nb_{0.15}O_3$ ($x=0$ and 0.05) were synthesized by the conventional solid-state reaction method. The X-ray diffraction showed that these compounds crystallized, at room temperature, in the orthorhombic structure with Pbnm space group. The scanning electron microscopy analysis showed a decrease in grain size with the La^{3+} substitution rate. Through the diffuse reflectance spectroscopy, we extracted the band gap energy, which decreases with the addition of La^{3+}, which implies the improvement of the semiconductor behavior. Filament, a study on the dielectric properties, in the frequency range from 1 kHz to 1 MHz, of our samples, shows that the substitution of calcium and potassium by lanthanum in A site introduced an improvement to these properties and the appearance of a new transition.

Keywords Perovskite · X-ray diffraction · Reflectance · Permittivity

1 Introduction

Perovskite is a kind of crystal structure with general formula ABX_3, which has been used in a variety of applications as in photovoltaic (for hybrid perovskite materials) [1, 2]. In particular, the perovskites of formula ABO_3 remain interesting because of their multifunctional properties such as: FE properties (non-volatile memories), important permittivities (capacitors), large piezoelectric (PZ) effects (sensors, actuators, etc.), and important pyroelectric coefficient (infrared detectors) [3–7]. As a result, most researchers are concerned with improving these dielectric properties rather than looking at new syntheses. The use of lead-based materials, the best known of which is PZT ($Pb(Zr_{1-x}Ti_x)O_3$), allowed us to carry out the first studies and the first applications using PZ properties. These materials are widely used because of their FE and PZ properties. However, for environmental reasons, especially because of pollution from industry, there is a tendency to limit the use of lead until it can be banned altogether. Therefore, we are on the quest for multifunctional materials, alternative lead-free having the same properties as PZT [8, 9].

Calcium titanate ($CaTiO_3$, CT) ceramic is renowned for several years, thanks to its applications as a catalyst in the conversion of light hydrocarbons [10], in the treatment and storage of nuclear waste [11], capacitor or resonators [12], production of optical discs with very high storage density [13], manufacture of medical prostheses [14]. Generally, the dielectric properties of the CT are enhanced by appropriate substitutions of the Ca^{2+} and/or Ti^{4+} cations in the perovskite lattice by other types of cations [15, 16].

Based on these considerations, the main objectives of our work were, first of all, the elaboration, by classical solid way, of homogeneous solutions $Ca_{0.85-x}La_xK_{0.15-x}Ti_{0.85}Nb_{0.15}O_3$ ($x=0$ and 0.05). Then, we focused on the physico-chemical characterization of these new FE ceramics or relaxers of perovskite structure. Structural properties were investigated by X-ray diffraction (XRD) and the scanning electron microscope (SEM). Then, we studied the optical and dielectric characteristics of these materials.

✉ Hend Kacem
kacem.hend@gmail.com

[1] Laboratoire de Physique Appliqué, Faculté des Sciences de Sfax, Université de Sfax, B.P. 1171, 3000 Sfax, Tunisia

[2] Laboratoire de la Matière Condensée et des Nanosciences, LR11ES40, Faculté des Sciences de Monastir, Université de Monastir, 5000 Monastir, Tunisia

2 Experimental details

The polycrystalline $Ca_{0.85-x}La_xK_{0.15-x}Ti_{0.85}Nb_{0.15}O_3$ ($x=0$ and 0.05) samples were synthesized by the conventional solid-state reaction method, with high-purity oxide powders $CaCO_3$ (99%), K_2CO_3 (99.99%), TiO_2 (99%), Nb_2O_5 (99.99%) and La_2O_3 (99.5%) as starting raw materials. First of all, the raw powders are weighed by stoichiometry and then they are ground for 2 h in ethanol with an agate mortar. After drying, these powders were calcined for 24 h at 900 °C. The powders obtained are again grounded for 2 h and are compressed into discs with a diameter of 8 mm. Finally, these pellets were sintered at 1200 °C for 24 h. XRD of all the samples were recorded in the 2θ range from 10° to 80° for structural analysis and phase determination. The microstructure was determined by SEM (JEOL JSM.6390L). The reflectance measurements were obtained using an ocean optic spectrometer (2000 USB) in the wavelength range from 300 to 1000 nm. Concerning the dielectric properties, we used the Wayne-Kerr 6425 component analyzer to determine the dielectric constant (εr) and the loss ($\tan\delta$) as a function of temperature (300–800 K) for different frequencies (1 kHz–1 MHz).

3 Results and discussion

3.1 X-ray diffraction

To describe the structural properties of our compounds, we carried out, at room temperature, XRD analysis. Figure 1 shows the dependence of XRD patterns of $Ca_{0.85-x}La_xK_{0.15-x}Ti_{0.85}Nb_{0.15}O_3$ ($x=0$ and 0.05) ceramics. It was confirmed that the matrix phase is $CaTiO_3$ identified by the software "X'Pert HighScore Plus". It was also observed that the second phase of TiO_2 (Rutile) was formed in all samples (marked by "."). The formation of TiO_2 can be associated with the following factors:

- Due to the high volatility of potassium at high temperatures (800 and 850 °C, respectively), segregation of Ti^{4+} ions is observed.
- According to Hennings and Schreinemacher [17], it is likely that Ca^{2+} cations can be substituted for Ti^{4+} cations at $Ca_{0.85-x}La_xK_{0.15-x}Ti_{0.85}Nb_{0.15}O_3$ B sites. When the latter occurs, a Ca''_{Ti} defect is generated leading to the formation of an oxygen deficiency ($V^{\bullet\bullet}_O$) according to the following reaction:

$$Ti^x_{Ti} + O^x_o + CaO \rightarrow Ca''_{Ti} + V^{\bullet\bullet}_O + TiO_2. \quad (1)$$

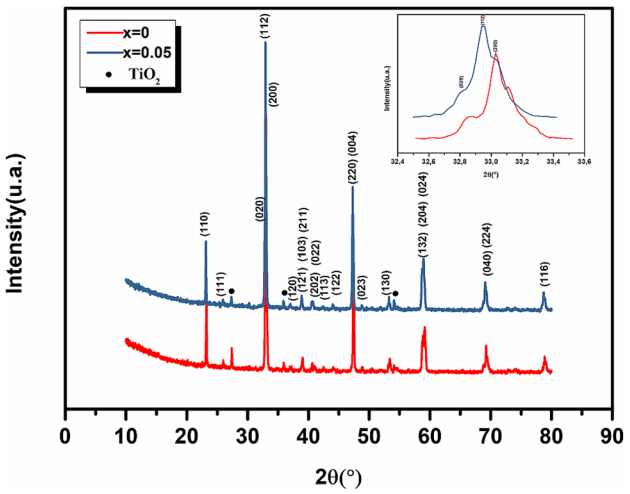

Fig. 1 Room temperature powder XRD for $Ca_{0.85-x}La_xK_{0.15-x}Ti_{0.85}Nb_{0.15}O_3$ ($x=0.00$ and 0.05). The inset is an enlargement of the scale of the most intense peak

Thus, based on this reaction (1), when the Ti^{4+} cations are replaced by Ca^{2+} cations, a large amount of TiO_2 is produced. However, in our case, it is often difficult to discard the Ti^{4+} cation from the center of the TiO_6 octahedron, especially since the radius of the Ca^{2+} cation (coordination 6, $R_{Ca^{2+}} = 1.00$ Å) is much greater than that of Ti^{4+} (coordination 6, $R_{Ti^{4+}} = 0.605$ Å). In addition, XRD analyses confirm the presence of Ca^{2+} cations in A sites. Therefore, it can be said that potassium evaporations during sintering may be responsible for the presence of the TiO_2 phase.

An enlargement of the scale of the most intense peak of the common phase of two compounds, shown in inset Fig. 1, presents that depending on the substitution rate x, the angular position of Bragg shifts to the small angles, a sign of an increase in the volume of the mesh. In addition to a slight enlargement, a sign of a slight decrease in the size of the crystalline grains was observed. The structure refinement was carried out by Rietveld analysis (see Fig. 2a, b). The main phase has been refined in orthorhombic symmetry in the Pbnm space group, with Wyckoff atomic positions: 4c (x, y, 1/4) for (Ca/La/K), 4b (0, 0.5, 0) for (Ti/Nb), 4c (x, y, 1/4) for O_1 and 8d (x, y, z) for O_2, and in the P42/mnm space group for the TiO_2 secondary phase. The refined structural parameters are listed in Table 1.

To explain the overall compactness, stability and the existence of distortions in the perovskite structure, Goldschmidt suggests a tolerance factor (t) which is expressed by the following relation [18]:

$$t = \frac{\langle r_A \rangle + r_O}{\sqrt{2}\left(\langle r_B \rangle + r_O\right)}, \quad (2)$$

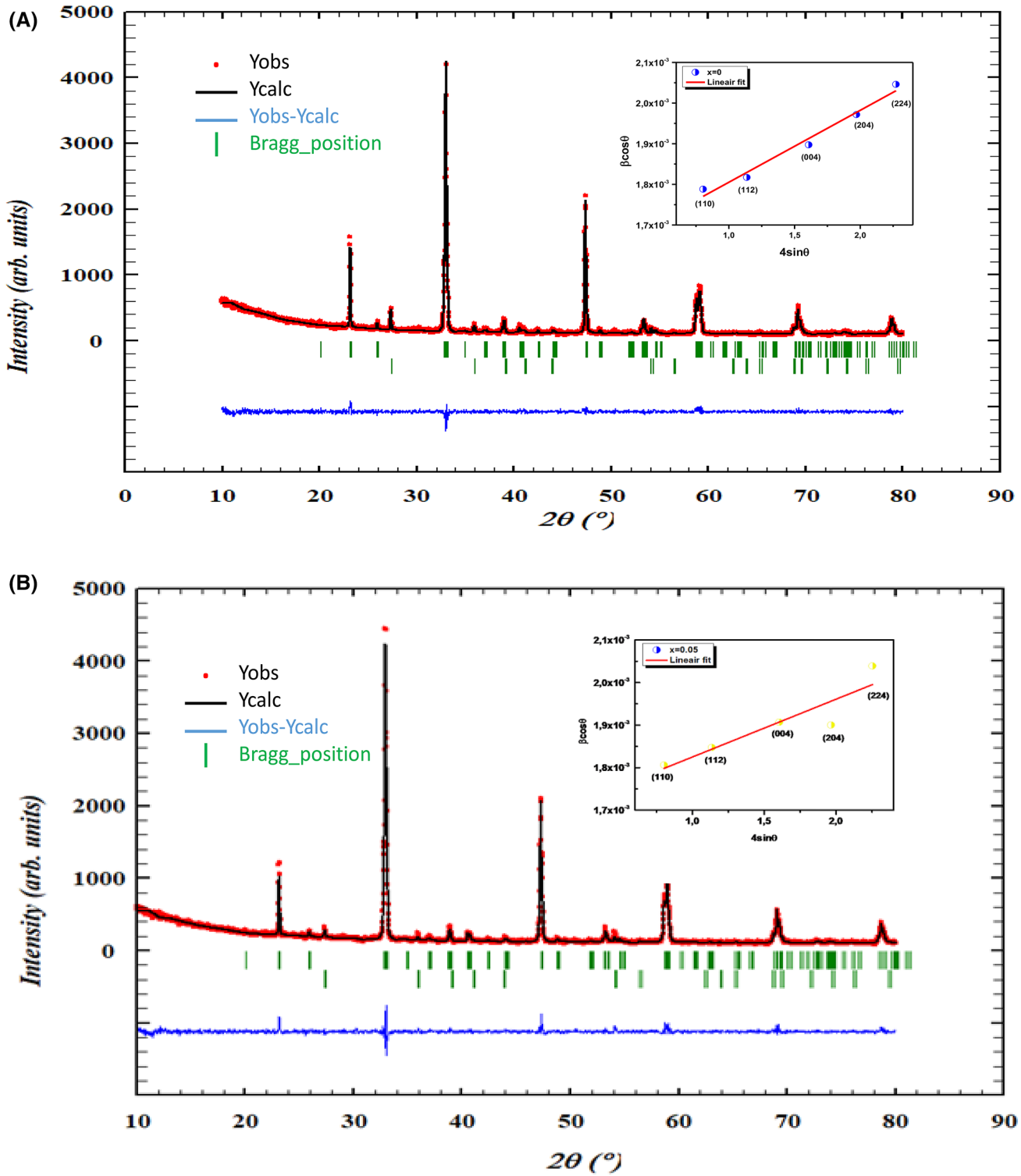

Fig. 2 Rietveld plots of XRD data for $Ca_{0.85-x}La_xK_{0.15-x}Ti_{0.85}Nb_{0.15}O_3$ with **a** $x=0.00$ and **b** $x=0.05$ ceramics. Inset shows their corresponding strain graph

where $\langle r_A \rangle$, $\langle r_B \rangle$ and r_O are the ionic radii [19]. The perovskite structure only exists if $0.75 \leq t \leq 1.06$ and, depending on its value, more or less distorted cubic structures are observed. If $t=1$, then, the structure is ideal cubic. Thus, the deviation of the factor from the ideal value explains the internal deformation in the perovskites. In our case

Table 1 Structural parameters obtained from Rietveld refinements of the XRD pattern

x	0.00	0.05
Space group	Pbnm	Pbnm
a (Å)	5.400 (3)	5.413 (2)
b (Å)	5.4524 (3)	5.4538 (2)
c (Å)	7.669 (4)	7.680 (4)
V (Å^3)	225.837 (2)	226.723 (2)
Ca/La/K atomic positions		
x	−0.008 (16)	−0.009 (16)
y	0.032 (9)	0.025 (11)
z	0.25	0.25
Ca/La/K Biso (Å^2)	1.645 (5)	0.74486 (3)
Ti/Nb atomic positions		
x	0	0
y	0.5	0.5
z	0	0
Ti/Nb Biso (Å^2)	0.021 (9)	0.271 (1)
O(1) atomic positions		
x	0.081 (3)	0.069 (3)
y	0.485 (3)	0.487 (4)
z	0.25	0.25
O(1) Biso (Å^2)	0.406 (2)	0.540 (4)
O(2) atomic positions		
x	0.714 (2)	0.719 (3)
y	0.288 (18)	0.287 (2)
z	0.036 (17)	0.032 (20)
O(2) Biso (Å^2)	0.17299 (3)	0.489 (8)
Agreement factors		
R_P (%)	6.79	6.66
R_{WP} (%)	8.62	8.34
R_F (%)	5.68	6.33
χ^2	1.32	1.18
%Cont	94.7/5.3	96.81/3.19

$0.75 < t < 1$, therefore, the perovskite structure persists (see Table 4).

The crystallite size has been estimated using different methods such as Scherrer's formula and Williamson–Hall's method (W–H). The Scherrer's formula can be expressed by:

$$\beta_{\text{size}} = \frac{0.9\lambda}{D_s \cos\theta}, \tag{3}$$

where D_s, β, λ, and θ are the crystallite size, the full width at half maximum (FWHM), the wavelength of CuKα radiation ($\lambda = 1.5406$ Å) and the Bragg's diffraction angle of the most intense peak, respectively. When calculated the FWHM ($\beta = \sqrt{\beta_{\text{obs}}^2 - \beta_{\text{ins}}^2}$). We take into account the instrumental broadening (β_{ins}) factor that was taken 0.001013373°. This formula is used to determine, from a measured diffraction width, the crystallite size, and therefore other sources of broadening and the existence of defects in the lattice are neglected [20]. In turn, this leads to an underestimation in a severe way of size [21]. Table 2 presents the value of D_s.

Table 2 Calculated grains size and crystallites size of $Ca_{0.85-x}La_xK_{0.15-x}Ti_{0.85}Nb_{0.15}O_3$ with $x = 0.00$ and $x = 0.05$

x	D_S (nm)	D_{WH} (nm)	D_{SEM} (μm)
0	74	85	2.68
0.05	73	82	1.46

Nevertheless, WH's method [22] consists of finding lattice deformation and an average size of coherently diffracting domains, which can be expressed in the form of:

$$\frac{\beta_i \cos\theta_i}{\lambda} = \frac{0.9}{D_{\text{WH}}} + \frac{4\varepsilon \sin\theta_i}{\lambda}, \tag{4}$$

where ε ($= \frac{\Delta d}{d}$) is the elastic strain. The inset of Fig. 2a, b shows $\beta_{hkl} \cos\theta$ versus $4\sin\theta$. From the values of the intercept on the y-axis, the average crystal sizes are found in Table 2. It was found that the average crystal sizes determined by the different methods are always decreasing. This indicates that incorporation of lanthanum into the A site inhibits the grain growth.

To take an idea of the dispersion of the material (the grains constituting the ceramics), the micrographs of our samples represented in Fig. 3a, b were obtained using SEM. From these images (Fig. 3a, b), we can see that the grain morphology varies according to the substitution rate for La^{3+} and that the grains are joined with a virtual absence of porosity. According to Image J software, the average particle size of the compounds has been estimated. After that, we can fit the data obtained with the log-normal function [23]:

$$f(D) = \frac{1}{\sqrt{2\pi}\sigma D} \exp\left(-\frac{\ln\left(\frac{D}{D_0}\right)^2}{2\sigma^2}\right), \tag{5}$$

where D_0 and σ are the median diameter collected from the SEM and the data dispersions, respectively. Figure 3c, d shows the dispersion histogram. The mean diameter $< D \geq D_0 \exp\left(\frac{\sigma^2}{2}\right)$ and standard deviation $\sigma_D = \langle D \rangle \left[\exp\sigma^2 - 1\right]^{\frac{1}{2}}$ were determined using fit results. The average particle sizes are summarized in Table 2.

3.2 Diffuse reflectance spectroscopy

To study the diffuse reflectance measurement (see Fig. 4), the values of R_∞ were expressed in terms of values $F(R_\infty)$

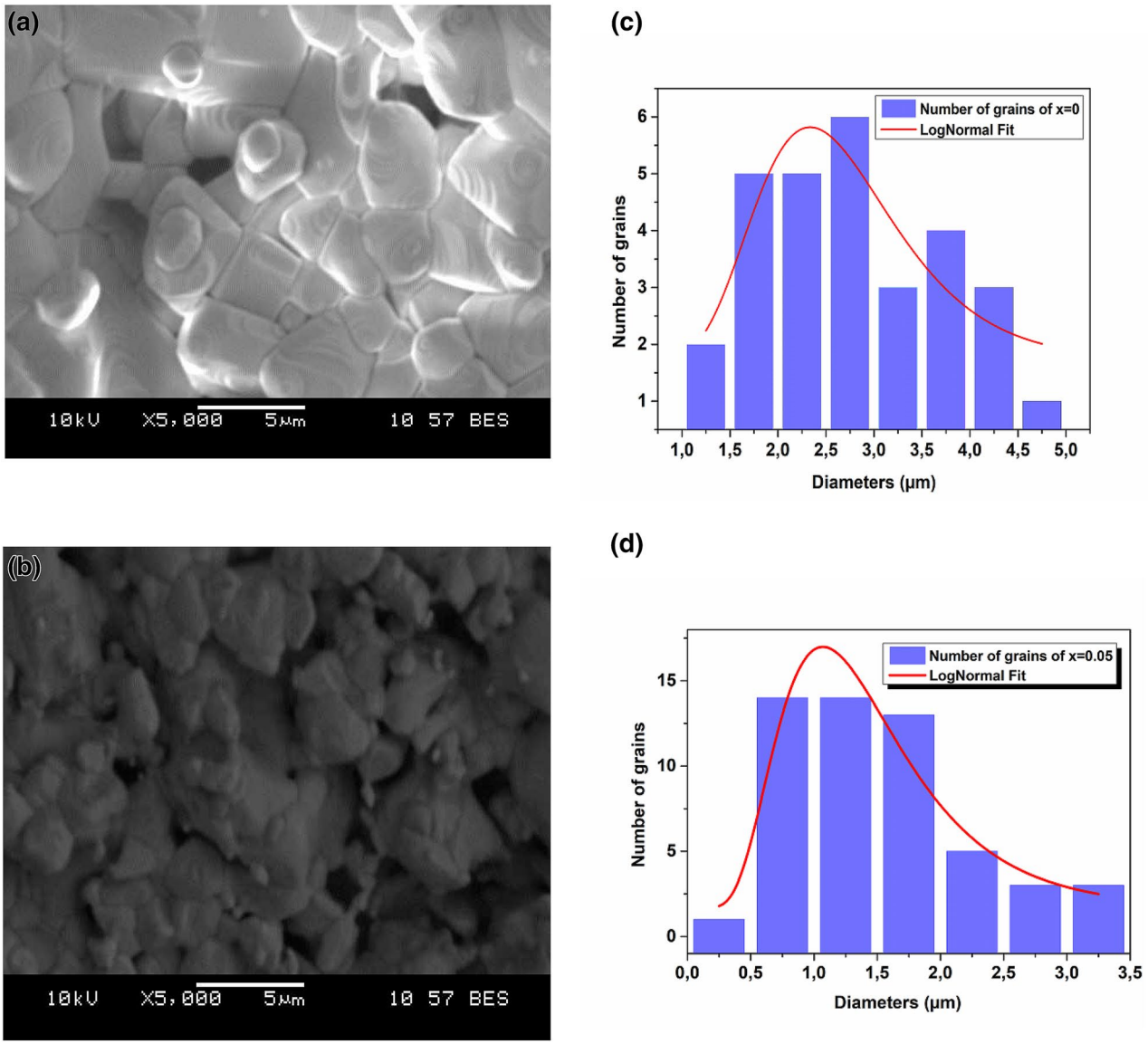

Fig. 3 SEM image of $Ca_{0.85-x}La_xK_{0.15-x}Ti_{0.85}Nb_{0.15}O_3$ with **a** $x=0.00$ and **b** $x=0.05$. **c** and **d** histograms of average grains size for $x=0.00$ and $x=0.05$, respectively

according to the Kubelka–Munk equation, which is described by [24]:

$$F(R_\infty) = \frac{k}{S} = \frac{(1-R_\infty)^2}{2R_\infty}, \tag{6}$$

where k and S are the absorption and scattering coefficient, respectively. According to the Tauc equation related to the incident photonic energy ($h\nu$) and to the absorption coefficient (α) given by the following equation $(\alpha h\nu)^2 \propto A(h\nu - E_g)$, we can determine the values of the band transition gap E_g. The E_g values are summarized in Table 3.

The unit cell distortion and the impurity provoke a defect in the band, which elevates the intermediary levels within the band gap region. Furthermore, the width of defect bands, which are formed in the band gap, is related to the Urbach tail [25]. The equation [25, 26] (see Fig. 5) can describe it:

$$\alpha = \alpha_0 \exp\left(\frac{h\nu}{E_U}\right), \tag{7}$$

where α_0 and E_U are constant and the Urbach energy, respectively. This energy can be utilized to characterize the degree of disorder in crystalline and amorphous solids and demonstrate the width of the band tails of the localized states. The E_U values are also summarized in Table 2. The addition of La^{3+} ions produces a slight increase in the Urbach energy

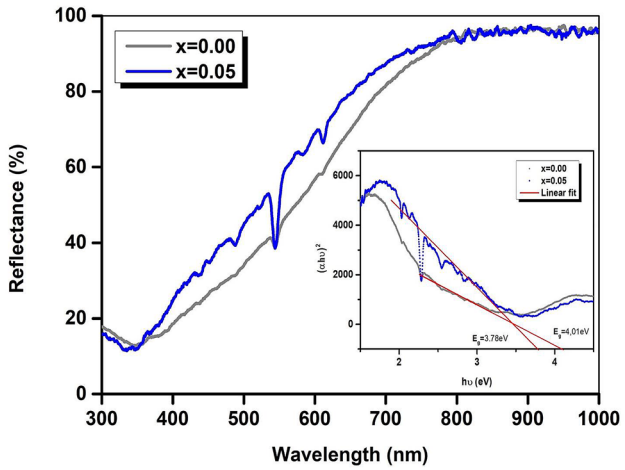

Fig. 4 Diffused reflectance spectrum of $Ca_{0.85-x}La_xK_{0.15-x}Ti_{0.85}Nb_{0.15}O_3$ ($x=0.00$ and 0.05) powders. The inset is band gap analysis of $Ca_{0.85-x}La_xK_{0.15-x}Ti_{0.85}Nb_{0.15}O_3$ ($x=0.00$ and 0.05) ceramics

Table 3 Band gap energy E_g and Urbach energy E_U for $Ca_{0.85-x}La_xK_{0.15-x}Ti_{0.85}Nb_{0.15}O_3$ ($x=0.00$ and 0.05) ceramics

x	0.00	0.05
E_g (eV)	4.01	3.78
E_U (eV)	0.87	0.92

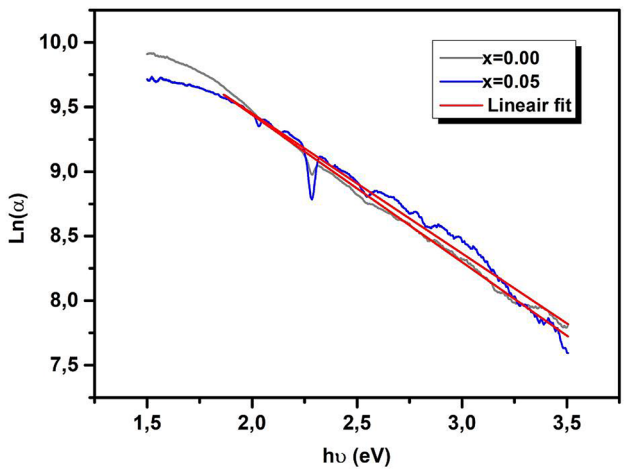

Fig. 5 Plot ln(α) versus photon energy (hv) for $Ca_{0.85-x}La_xK_{0.15-x}Ti_{0.85}Nb_{0.15}O_3$ ($x=0.00$ and 0.05)

values. This result certainly indicates the intermediate states' formation in the band gap and a reduction in the gap values.

3.3 Dielectric studies

Following the reflectance measurements, we discussed the dielectric properties of our samples. Figure 6 displays the temperature dependence of relative permittivity measured at various frequencies from 300 to 800 K. Three obvious dielectric peaks were observed for the samples of $x=0.00$ and 0.05. They originated from phase transitions, corresponding to rhombohedral–orthorhombic (R–O) ($T_1=T_{R-O}$), orthorhombic–tetragonal (O–T) ($T_2=T_{O-T}$) and tetragonal–Cubic (T–C) (T_m), similar to those of $KNbO_3$ ceramic [27]. Additionally, it is important to note that the ε_r' curve of the La_2O_3 substituted sample shows an abnormal phenomenon than pure CKTN. The insertion of La_2O_3 into A site transforms the dielectric peak T_m of the pure compound CKTN into two peaks (defined as T_{m1} and T_{m2}). The appearance of the abnormal dielectric peak might be ascribed to the maximum dielectric peak is displaced, and the second dielectric peak appeared at temperature T_{m2}, which arises from the composition fluctuation resulting from the insertion of La_2O_3. The same phenomenon has been reported in $BaTiO_3$–$Bi(Mg0.5Zr_{0.5})O_3$ and $BaTiO_3$–$BiScO_3$ ceramics. This is due to related to a layer full of Zr, Mg, and Bi relative to the grain interior [28, 29].

On the other hand, the peak T_m moves towards high temperature when the La^{3+} content increases. It may be related to t [18]. The reduced of t (see Table 4) value is often related to T_m [30]. In other words, T_m shows an upward trend when the low substitution of La^{3+} in A site contributes a lower t value [31]. T_{R-O} and T_{O-T} increase with La^{3+} content. Based on the Thomas' theory of the stability of FE domain [32], FE domains are highly dependent on the ferroelectrically active [BO_6] octahedral and the coupling of A-site cations in ABO_3-type perovskite structure. From the point of crystal structure, the forming of A-site vacancies because of La^{3+} substituted is favorable to the magnitude of coupling between [BO_6] octahedral and A-site cations [33].

The dielectric behavior is further analyzed by the modified Curie–Weiss [34]:

$$\frac{1}{\varepsilon_r'}-\frac{1}{\varepsilon_{rm}'}=\frac{(T-T_m)^{\gamma}}{C'}, \tag{8}$$

where ε_{rm}' and T_m are, respectively, the values of the real permittivity and the temperature of the peak. The factor γ reflects the diffuse nature of the phase transition. Its value is 1 for conventional FE and 2 for ideal diffuse behavior. Indeed, the results reveal (see Fig. 7) that the diffusion factor varies, in increasing order, from 1.61 to 1.63, respectively, for the compositions $x=0$ and 0.05, indicating that the relaxing effect improves with the increase of substitution rate.

The portraying parameter of diffuseness degree 'D' is related to the temperature interval where the volume of polar microscopic regions changes as a result of the emergence of new microscopic Polar Regions. This is really prescribed as [35]:

$$D=T_{\left(\frac{\partial\varepsilon_r'}{\partial T}\right)_{min}}-T_{\left(\frac{\partial\varepsilon_r'}{\partial T}\right)_{max}}, \tag{9}$$

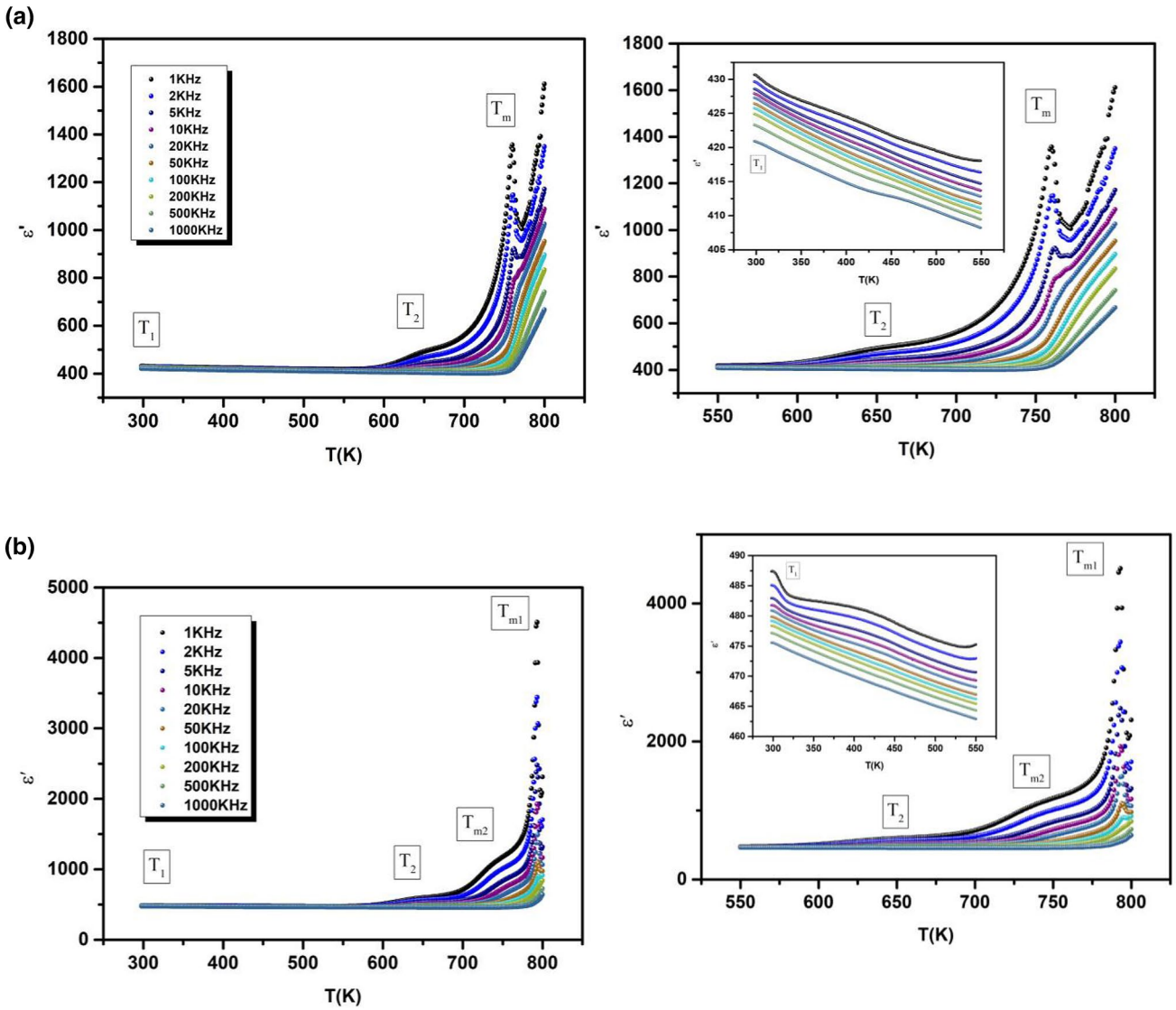

Fig. 6 Temperature and frequency dependence of the real part of permittivity for the compositions **a** $x=0.00$ and **b** $x=0.05$

Table 4 Parameters obtained from the temperature dependence of dielectric permittivity for $Ca_{0.85-x}La_xK_{0.15-x}Ti_{0.85}Nb_{0.15}O_3$ ($x=0.00$ and 0.05) ceramics

x	0.00	0.05
T_2 (K)	650	639
T_m/T_{m1} (K)	760	792
T_{m2} (K)	–	739
ε_m (T_m/T_{m1})	1357	4505
t (tolerance factor)	0.97	0.95
γ	1.61	1.63
D		
T_2	36	49
T_m/T_{m1}	6	29
T_{m2}	–	4

where $T_{\left(\frac{\partial \varepsilon_r'}{\partial T}\right)_{min}}$ and $T_{\left(\frac{\partial \varepsilon_r'}{\partial T}\right)_{max}}$ are the temperature when $\frac{\partial \varepsilon_r'}{\partial T}$ reaches the minimum and maximum, respectively. Figure 8 represents the schematic curve of $\frac{\partial \varepsilon_r}{\partial T}$ against (T) for the two peaks: T_2 and T_m for $x=0$ and three peaks: T_2, T_{m1} and T_{m2} for $x=0.05$. The temperature interval between $T_{\left(\frac{\partial \varepsilon_r'}{\partial T}\right)_{min}}$ and $T_{\left(\frac{\partial \varepsilon_r'}{\partial T}\right)_{max}}$ reflects the diffuseness degree microscopically. The vertical dashed lines in Fig. 8a, b correspond to $T_{\left(\frac{\partial \varepsilon_r'}{\partial T}\right)_{min}}$ and $T_{\left(\frac{\partial \varepsilon_r'}{\partial T}\right)_{max}}$ values. D is the interval between $T_{\left(\frac{\partial \varepsilon_r'}{\partial T}\right)_{min}}$ and $T_{\left(\frac{\partial \varepsilon_r'}{\partial T}\right)_{max}}$. The values of "$D$" are regrouped in Table 4.

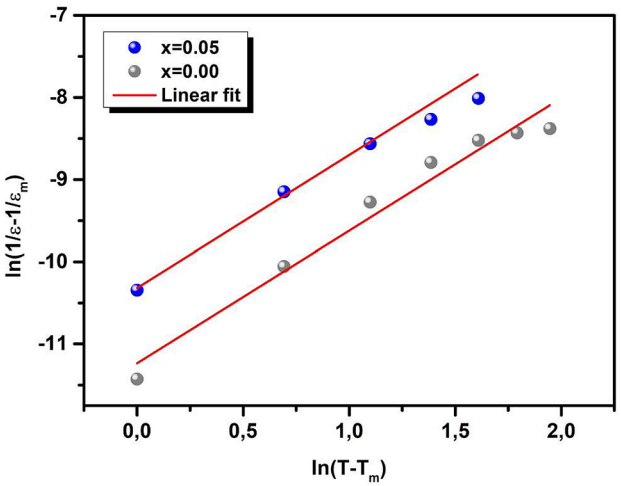

Fig. 7 Plots of $\ln\left(\frac{1}{\varepsilon'}-\frac{1}{\varepsilon'_r}\right)$ as a function of $\ln(T-T_m)$at 1 kHz for the compositions **a** $x=0.00$ and **b** $x=0.05$

It was found that the values of 'D' decrease with the temperature increase. This indicates that the transition that occurred with the less diffuse disorder is the phase transition from paraelectric-FE; whereas, the transition that occurred with the more diffuse disorder is the phase transition tetragonal to the orthorhombic phase transition.

Figure 9a, b shows the thermal variation of the dissipation factor (tan δ) at different frequencies for the two compositions $x=0$ and 0.05, respectively. The overall appearance shows that all the anomalies T_1, T_2, T_{m1}, and T_{m2} were already detected by the evolution of the dielectric permittivity of each composition.

For high temperatures $T>T_m$, all ceramics show a sudden increase in dielectric loss, especially for low frequencies. This can be attributed to a shift of thermally activated charge carriers such as the space charge, usually observed in systems with local composition and electrical inhomogeneity [36] which in our case can come from the insertion of potassium and lanthanum in site A and niobate in site B.

The temperature dependence of the electrical conductivity σ' of our samples ($x=0.00$ and 0.05) is represented in

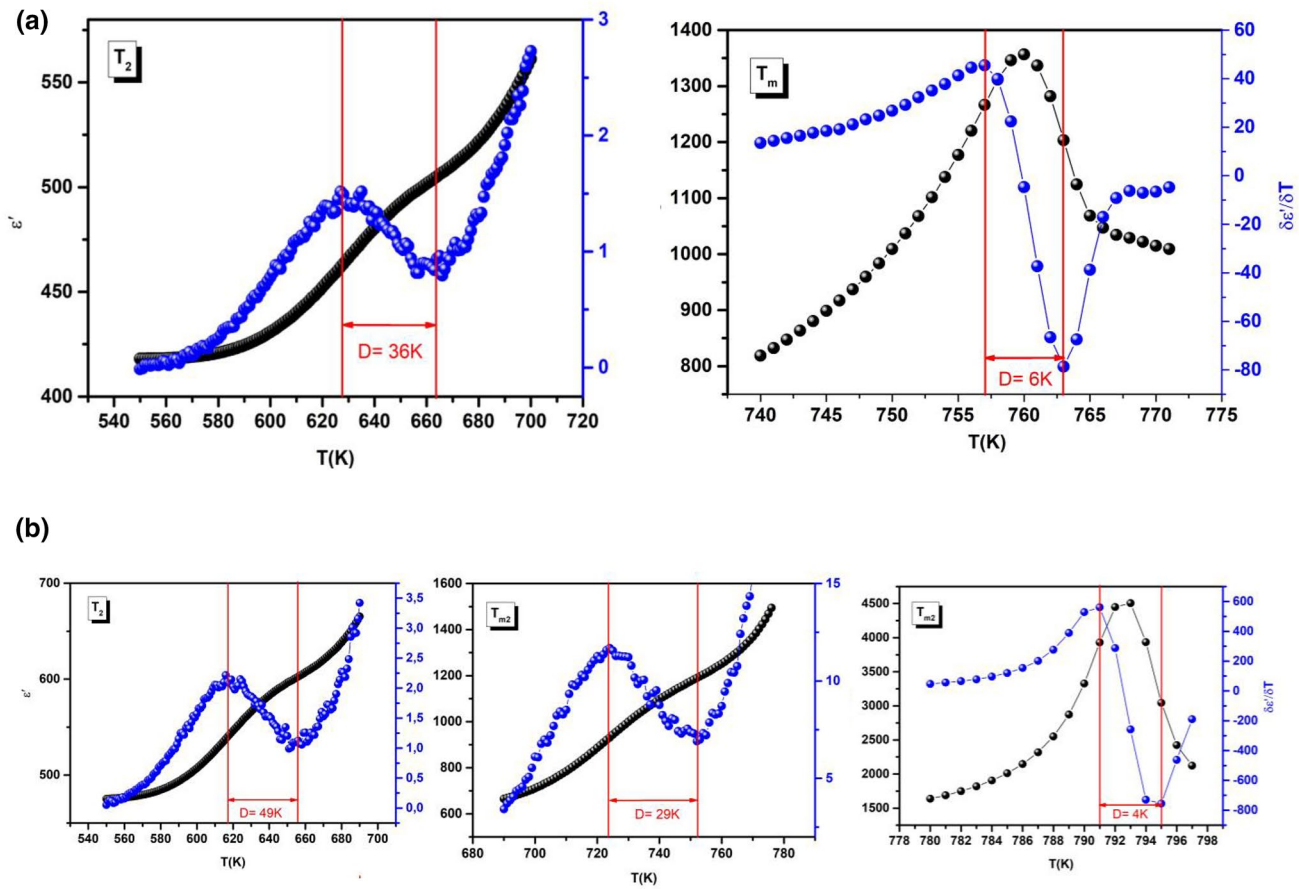

Fig. 8 Determining the values of D by variation of $\left(\frac{\delta\varepsilon}{\delta T}\right)$ of $Ca_{0.85-x}La_xK_{0.15-x}Ti_{0.85}Nb_{0.15}O_3$ with **a** $x=0.00$ and **b** $x=0.05$

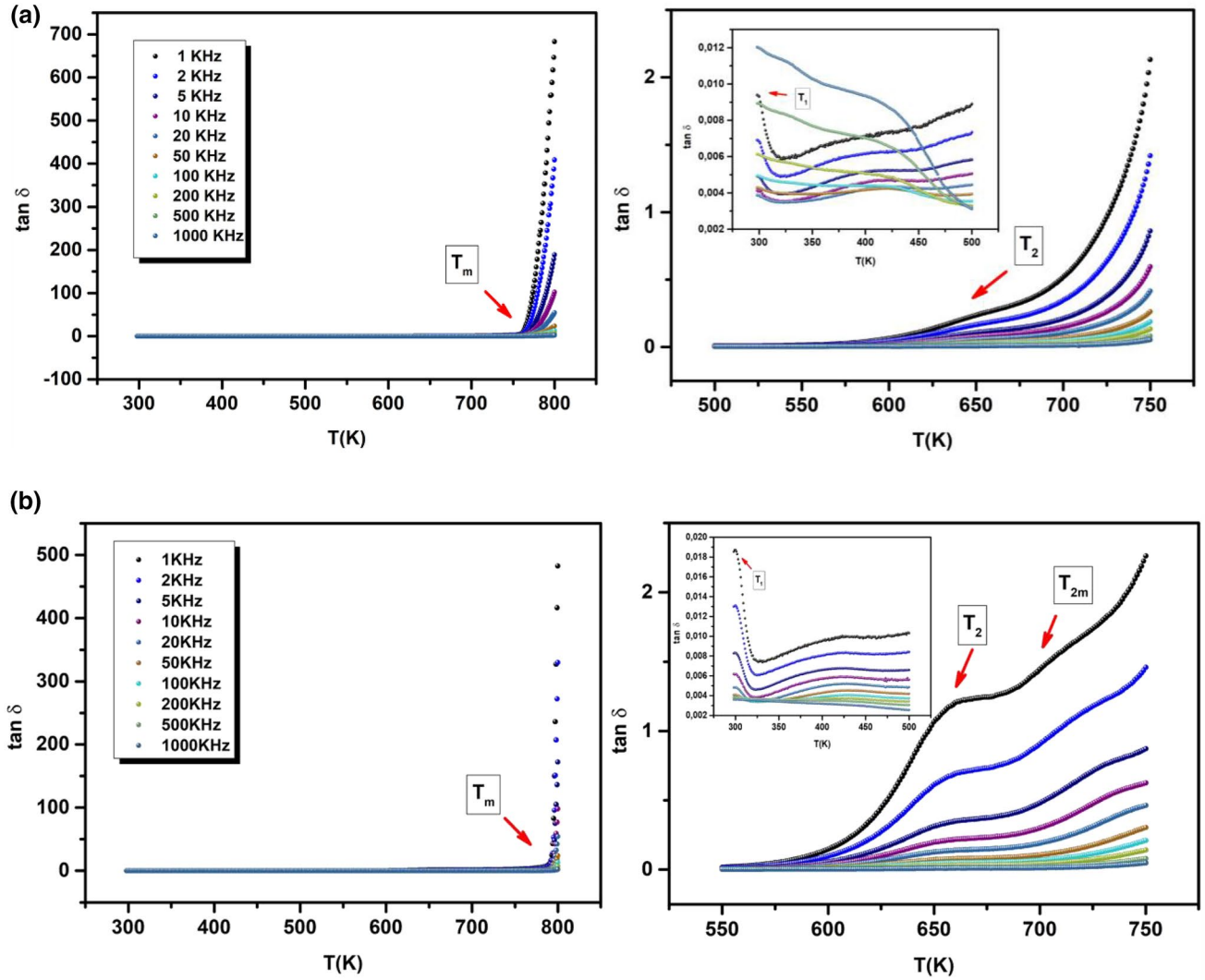

Fig. 9 Temperature and frequency dependence of the dielectric loss (tan δ) for compositions **a** $x = 0.00$ and **b** $x = 0.05$

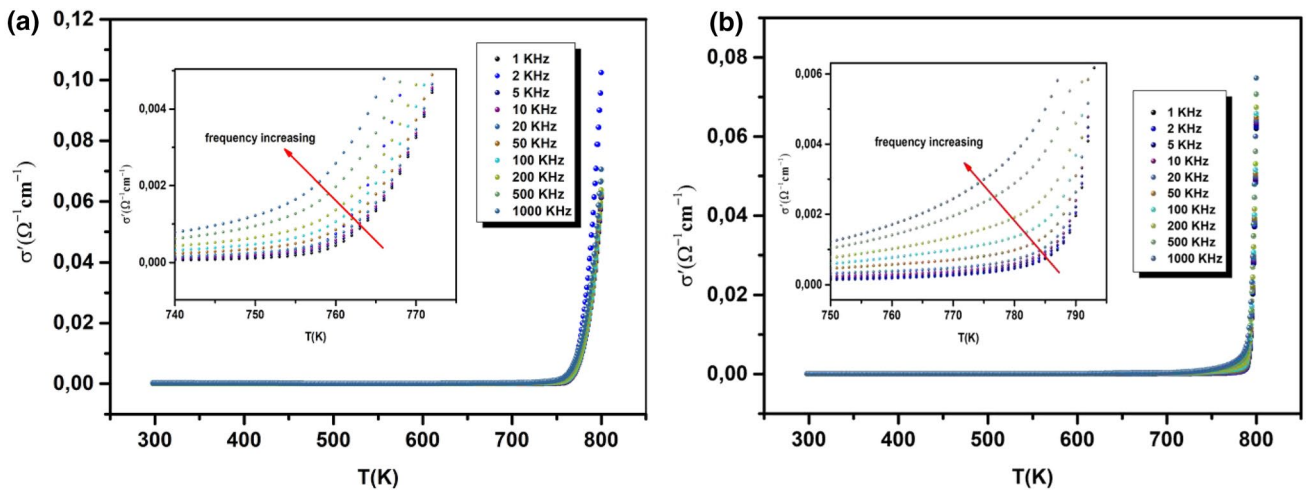

Fig. 10 Temperature and frequency dependence of dielectric conductivity for compositions **a** $x = 0.00$ and **b** $x = 0.05$

Fig. 10 where σ' linked to the dielectric loss $\tan\delta$ with the formula:

$$\sigma' = 2\pi f \varepsilon_0 \tan\delta, \tag{10}$$

where f and ε_0 are the frequency and the permittivity of free space. The electrical conductivity increases with increasing of the frequency and temperature same time by expanding the frequency and temperature. So, a typical signature of the relaxation behavior is noted in the electrical conductivity curves. These results are concurrent with those obtained with the dielectric loss.

4 Conclusion

In this work, we have prepared and studied perovskite-type oxides with the general chemical formula: $Ca_{0.85-x}La_xK_{0.15-x}Ti_{0.85}Nb_{0.15}O_3$ ($x = 0.00$ and 0.05) ceramics. The development of these samples was produced by the solid–solid method. The structural studies carried out by XRD show that all the samples crystallize in an orthorhombic structure of Pbnm space group. The size of the grains changes with the level of substitution of lanthanum in site A and a decrease in steric distortion is observed. The band gap energy decreases with the addition of La^{3+}, which implies the improvement of the semiconductor behavior. Characterization by impedance spectroscopy shows that the two compositions are FE materials having a start of relaxation that can be induced by the inhomogeneity introduced by substituting different crystallographic sites.

References

1. T. Miyasaka, Bull. Chem. Soc. Jpn. **91**, 1058–1068 (2018)
2. Q. Jiang, Y. Zhao, X. Zhang, X. Yang, Y. Chen, Z. Chu, Q. Ye, X. Li, Z. Yin, J. You, Surface passivation of perovskite film for efficient solar cells. Nat. Photonics **13**, 460–466 (2019)
3. H.J. Noh, S.G. Lee, S.P. Nam, Y.H. Lee, Mater. Res. Bull. **45**(3), 339–342 (2010)
4. A.J. Bell, J. Eur. Ceram. Soc. **28**(7), 1307–1317 (2008)
5. J.W. Kim, D.C. Yoon, M.S. Jeon, D.W. Kang, J.W. Kim, H.S. Lee, Curr. Appl. Phys. **10**, 1297 (2010)
6. G. Zhang, S. Jiang, Y. Zhang, T. Xie, Curr. Appl. Phys. **9**(6), 1434–1437 (2009)
7. A.J. Moulson, J.M. Herbert, John Wiley & Sons (2003)
8. E. Ringgaard, T. Wurlitzer, J. Eur. Ceram. Soc. **25**(12), 2701–2706 (2005)
9. H. Du, F. Tang, D. Liu, D. Zhu, W. Zhou, S. Qu, Mater. Sci. Eng. B **136**(2–3), 165–169 (2007)
10. A.G. Andersen, T. Hayakawa, T. Tsunoda, H. Orita, M. Shimizu, K. Takehira, Catal. Lett. **18**(1–2), 37–48 (1993)
11. Y. Hanajiri, H. Yokoi, T. Matsui, Y. Arita, T. Nagasaki, H. Shigematsu, J. Nucl. Mater. **247**, 285–288 (1997)
12. R.P. Wang, C.J. Tao, J. Cryst. Growth **245**(1–2), 63–66 (2002)
13. L. Taibi-Benziada, A. Mezroua, R.V.D. Mühll, Ceram. Silik **48**(4), 180–183 (2004)
14. M. Manso, M. Langlet, J.M. Martınez-Duart, Mater. Sci. Eng. C **23**(3), 447–450 (2003)
15. A.B. Hassen, F.I.H. Rhouma, J. Dhahri, N. Abdelmoula, J. Alloy. Compd. **663**, 436–443 (2016)
16. C. Rayssi, S.E. Kossi, J. Dhahri, K. Khirouni, RSC Adv. **8**(31), 17139–17150 (2018)
17. D.F.K. Hennings, H. Schreinemacher, J. Eur. Ceram. Soc. **15**(8), 795–800 (1995)
18. G. Beskow, V.M. Goldschmidt, Geochemische Verteilungsgesetze der Elemente. Geologiska Föreningen i Stockholm Förhandlingar **46**(6–7), 738–743 (1924)
19. P. Xiao, Y. Guo, M. Tian, Q. Zheng, N. Jiang, X. Wu, D. Lin, Dalton Trans. **44**(39), 17366–17380 (2015)
20. B.R. Rehani, P.B. Joshi, K.N. Lad, A. Pratap, Indian J. Pure Appl. Phys. **44**, 157–161 (2006)
21. S. Britto, S. Joseph, P.V. Kamath, J. Chem. Sci. **122**(5), 751–756 (2010)
22. G.K. Williamson, W.H. Hall, Acta Metall **1**(1), 22–31 (1953)
23. M.H. Ehsani, T. Raouf, F.S. Razavib, J. Magn. Magn. Mater. **475**, 484–492 (2019)
24. H.M. Oo, H. Mohamed-Kamari, W.M.D. Wan-Yusoff, Int. J. Mol. Sci. **13**(4), 4623–4631 (2012)
25. M. Pant, D.K. Kanchan, N. Gondaliya, Mater. Chem. Phys. **115**(1), 98–104 (2009)
26. F. Urbach, Phys. Rev. **92**(5), 1324 (1953)
27. G. Shirane, H. Danner, A. Pavlovic, R. Pepinsky, Phys. Rev. **93**(4), 672 (1954)
28. H. Ogihara, C.A. Randall, S. Trolier-McKinstry, J. Am. Ceram. Soc. **92**(1), 110–118 (2009)
29. A. Zeb, S.J. Milne, J. Eur. Ceram. Soc. **34**(13), 3159–3166 (2014)
30. Q. Wang, H. Fan, C. Long, L. Huang, J. Mater. Sci. Mater. Electron. **25**(7), 2961–2968 (2014)
31. M. Chen, Z. Xu, R. Chu, Z. Wang, S. Gao, G. Yu, G. Li, Mater. Res. Bull. **59**, 305–310 (2014)
32. N.W. Thomas, J. Phys. Chem. Solids **51**(12), 1419–1431 (1990)
33. M. Chen, Q. Xu, B.H. Kim, B.K. Ahn, W. Chen, Mater. Res. Bull. **43**(6), 1420–1430 (2008)
34. N. Horchidan, A.C. Ianculescu, C.A. Vasilescu, M. Deluca, V. Musteata, H. Ursic, L. Mitoseriu, J. Eur. Ceram. Soc. **34**(15), 3661–3674 (2014)
35. C. Mao, X. Dong, G. Wang, S. Cao, C. Yao, J. Am. Ceram. Soc. **93**, 4011–4014 (2010)
36. H. Ghoudi, S. Chkoundali, A. Aydi, K. Khirouni, J. Appl. Phys. A **123**(11), 703 (2017)